

Improved B_0 field map estimation for high field EPI

Dirk H.J. Poot^{a,*}, Wouter Pintjens^a, Marleen Verhoye^{a,b},
Annemie Van Der Linden^b, Jan Sijbers^a

^aIBBT-Visionlab, University of Antwerp, 2610 Wilrijk, Belgium

^bBio Imaging Lab, University of Antwerp, 2020 Antwerpen, Belgium

Received 4 March 2009; revised 15 September 2009; accepted 6 December 2009

Abstract

Echo planar imaging (EPI) is an ultrafast magnetic resonance imaging (MRI) technique that allows one to acquire a 2D image in about 100 ms. Unfortunately, the standard EPI images suffer from substantial geometric distortions, mainly originating from susceptibility differences in adjacent tissues. To reduce EPI distortions, correction methods based on a field map, which is a map of the off-resonance frequencies, have been developed. In this work, a *nonlinear least squares estimator* is used to optimize the estimation of the field map of the B_0 field. The model of the EPI and reference data includes parameters for the phase evolution, the complex magnitude, the relaxation of the MRI signal and the EPI-specific phase difference between odd and even echoes, and from these parameters, additional corrections might be computed. The reference data required to estimate the field map can be acquired with a modified EPI-sequence. The proposed method is tested on simulated as well as experimental data and proves to be significantly more robust against noise, compared to the previously suggested method.

© 2010 Elsevier Inc. All rights reserved.

Keywords: Field mapping; Parameter estimation; Susceptibility artifacts; Echo planar imaging corrections

1. Introduction

Echo planar imaging (EPI) [1] is an ultrafast imaging technique, well suited for magnetic resonance imaging (MRI) applications that require high temporal resolution [e.g., functional MRI (fMRI)] or in which a large number of different images of the same object have to be acquired [e.g., Diffusion Tensor Imaging (DTI)] [2,3]. The main drawback of EPI is its sensitivity to off resonance factors such as B_0 field inhomogeneity, chemical shifts and eddy current effects from fast switching gradients. These effects introduce image artifacts, especially at high fields (7T and higher). Since high-field scanners are common in small animal imaging and are also starting to enter clinical applications, it is of major importance that correction strategies for EPI distortions are developed.

In the past, various methods to correct EPI distortions methods were proposed. These methods can be subdivided in three categories:

Acquisition. The first category of EPI distortion correction methods are methods that are applied at the hardware level during the acquisition. These methods commonly use shim coils, which generate spherical harmonic magnetic fields, to compensate for global and local field inhomogeneities. Conventional global shimming techniques try to optimize the field homogeneity for the entire imaged volume [4]. However, since the order of the spherical harmonic magnetic fields generated by the shim coils is limited, they cannot correct for all susceptibility differences in the brain. Dynamic shimming [5] has been shown to improve magnetic field homogeneity to a larger extent than conventional global shimming, since it optimizes the homogeneity of the main magnetic field by updating the shim settings for each slice separately. However, a drawback of dynamic shimming is the high performance of the shim coils that is required.

Registration. A second method to correct EPI distortions employs image registration [6] and post processing. For this method, a distortion free reference image, such as a spin echo (SE) image, is required. The EPI images are then registered to this reference image. Unfortunately,

* Corresponding author. Tel.: +32 3 265 24 58; fax: +32 3 265 22 45.
E-mail address: dirk.poot@ua.ac.be (D.H.J. Poot).

since field inhomogeneities cause local distortions, it is generally not possible to perform adequate corrections with affine transformations of the image only. Hence, more advanced, non-affine registration techniques are required. A drawback of these methods is that there might be insufficient contrast for the registration or the reference image might be of a different modality, which complicates the registration.

Field mapping. A last category of EPI distortion correction methods combines a special acquisition and post processing techniques. For these methods, extra reference data are acquired. From the reference data, a deformation field can be computed. This deformation field can then be used by post processing techniques to undo the deformations in the EPI images. Previously proposed methods that employ this approach measure the main field inhomogeneities [7–10], or the point spread function [10,11].

In this work, a technique from the last category, the field mapping technique, is optimized. For the standard field mapping [7], at least two images with different echo times have to be acquired. From the phase difference between these images, a field inhomogeneity map or off-resonance frequency map is calculated. To obtain reliable displacement maps, the standard field mapping requires the unwrapping of the phase discontinuities. A refinement of this method, which avoids the need for phase unwrapping, was proposed by Schmithorst et al. [8], who acquired multiple gradient echo (GRE) images to estimate the field map. However, due to the differences between even and odd EPI echoes, this method requires the reference data to be divided in two parts, containing either the echoes with odd or even echo number [15]. Moreover, relaxation effects were not taken into account.

We propose a new field mapping technique based on an improved model of the reference data along with a nonlinear least squares estimator. The model parameters represent properties of the MRI recording, the complex amplitude, the off-resonance frequency, the T_2^* relaxation, and the variation between even and odd EPI echoes. The proposed model does not require the splitting of the data in parts containing only the even and odd echoes prior to the estimation of the parameters. The performance in terms of the root mean square error (RMSE) and bias of this method is investigated by simulation and real data experiments. These experiments test the robustness to noise as well as the amount of reference data needed.

2. Methods

2.1. Field mapping

In magnetic resonance imaging, the demodulated magnetic resonance (MR) signal $S(t)$ of an excited volume Ω , generated by freely precessing nuclear spins in the presence of a linear magnetic field gradient \mathbf{G} , equals the Fourier transform of the effective density $\rho(\mathbf{r})$. This effective density

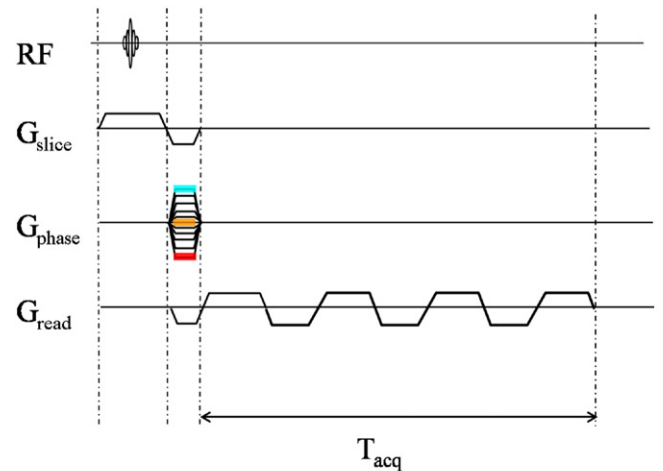
is the proton density weighted by the relevant decays (T_1, T_2, \dots) and contrasts (e.g., diffusion weighting), and in general, it is complex valued. When no distorting effects are present, the recorded signal is given by [12]

$$S(t) = \iint_{r \in \Omega} \rho(\mathbf{r}) e^{-ik(t) \cdot \mathbf{r}} d\mathbf{r}. \quad (1)$$

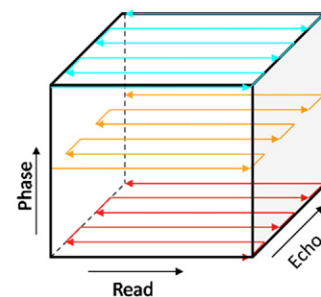
In Eq. (1), \mathbf{k} is a vector in k -space of which the components are given by

$$k_j(t) = \gamma \int_0^t \mathbf{G}(t') \cdot \mathbf{e}_j dt', \quad (2)$$

with $\mathbf{G}(t')$ the applied gradient at time t' ; γ , the gyromagnetic ratio; and \mathbf{e}_j , the cartesian unit vector in the direction j . From Eq. (1), it is clear that the image reconstruction involves an inverse Fourier transform, which can efficiently be computed when the signal is sampled on a regular grid in k -space, which it is EPI, when no samples are obtained during the gradient switching.



(A) Acquisition sequence



(B) Data cube

Fig. 1. (A) The sequence used for measuring the field map is a conventional EPI readout train, but the phase encoding gradient is replaced by the phase encoding gradient of a GRE sequence. (B) The data from the field map sequence is shown on a data cube. The color of the EPI train corresponds to the color of the selected phase encoding step from (A).

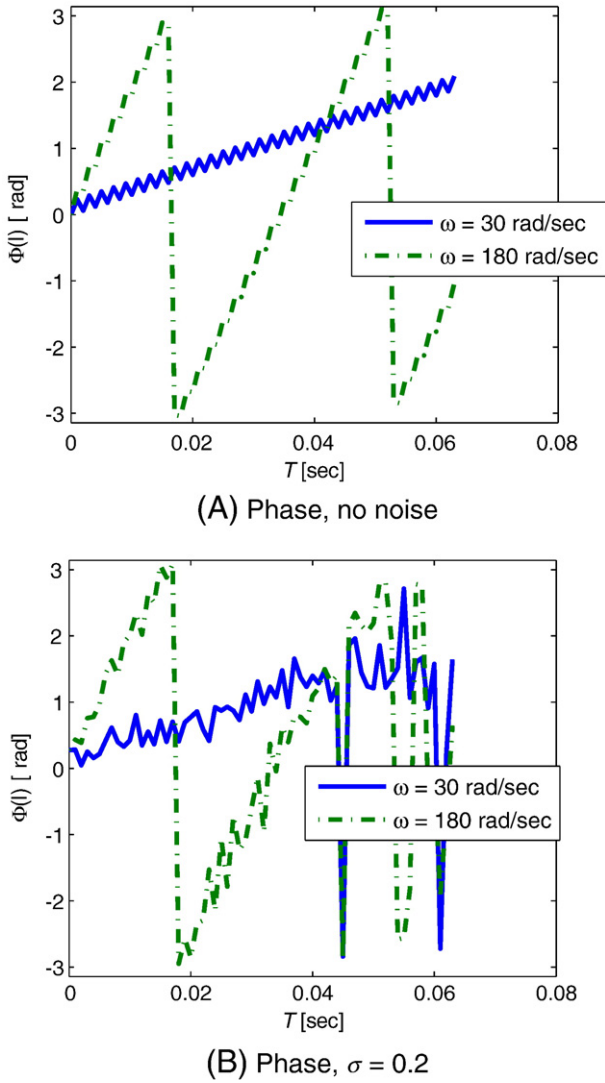


Fig. 2. One realisation of the phase of the simulated signals with both phase trends. No noise was added in panel (A); noise with $\sigma=0.2$ was added in panel (B).

In Eq. (1), it is assumed that only the gradients \mathbf{G} affect the acquired MR signal. However, in practice, additional factors such as timing offsets t_{off} , susceptibility effects causing an extra off-resonance frequency term $\omega(\mathbf{r})$, and T_2^* decay, affect the measured signal $S(t)$. Including these effects in Eq. (1) yields a more realistic model of the acquired MR signal:

$$\tilde{S}(t) = \iint_{r \in \Omega} \rho(\mathbf{r}) e^{-i[k(t + t_{\text{off}})\mathbf{r} - \omega(\mathbf{r})t] - \frac{t}{T_2^*}} d\mathbf{r}. \quad (3)$$

In a conventional EPI acquisition scheme the k -space is sampled line by line after one excitation. Hence, the off-resonance frequency $\omega(\mathbf{r})$ generally leads to a shift of the reconstructed position of $\rho(\mathbf{r})$, in the phase encoding direction. Since the field inhomogeneities, and therefore ω , are, by definition, not constant in Ω , these field inhomogeneities will

cause geometric distortions. By using reference data, $\omega(\mathbf{r})$ can be estimated and the geometric distortions can be corrected. In the next subsection, we will describe how the reference data is acquired.

2.2. Reference data

Reference data is acquired with an adjusted EPI sequence as shown in Fig. 1A. A standard EPI phase encoding scheme with N gradient echoes records a different k -space line with each echo. The echoes originate from the alternating amplitude of the read-out gradient, and the phase encoding gradient is used to select the line in k -space. However, in the sequence for the reference data acquisition, the EPI phase

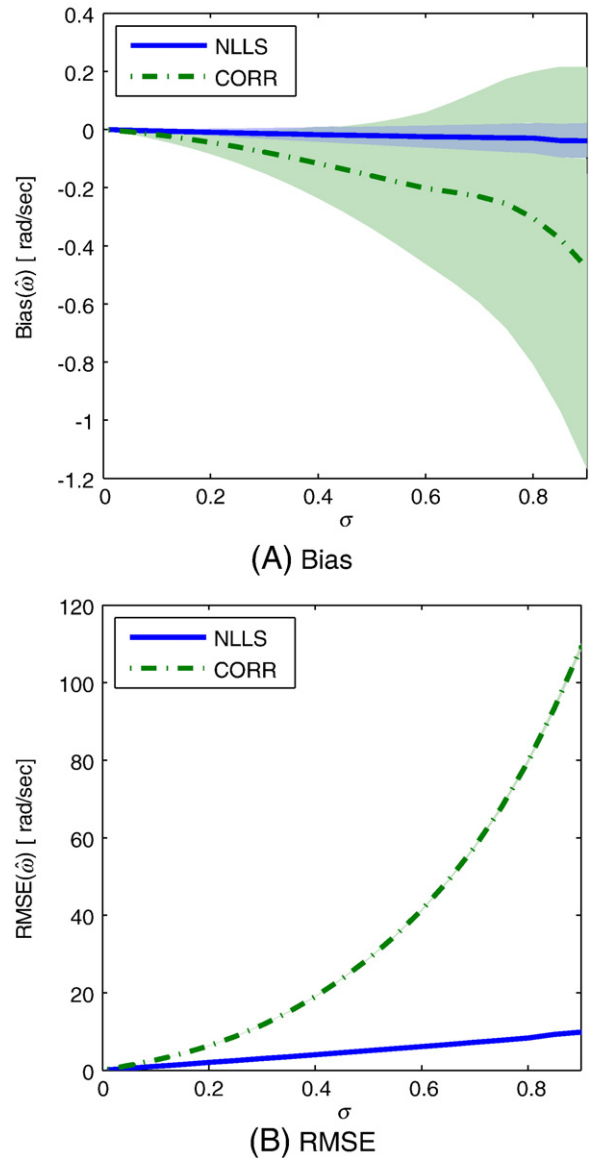


Fig. 3. The bias (A) and RMSE (B) of the CORR and the NLLS field map estimators from simulated data with $\omega=30$ rad/sec and $N=64$. The shaded areas represent the 95% confidence regions of the performance measures. For these simulations, $M=100000$ realizations were used.

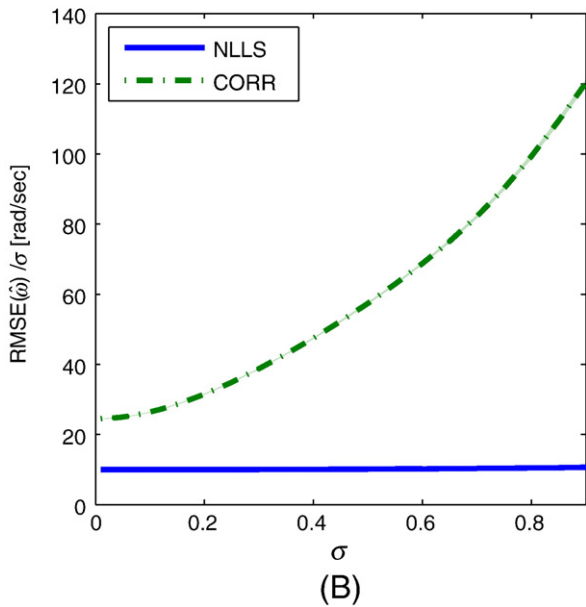
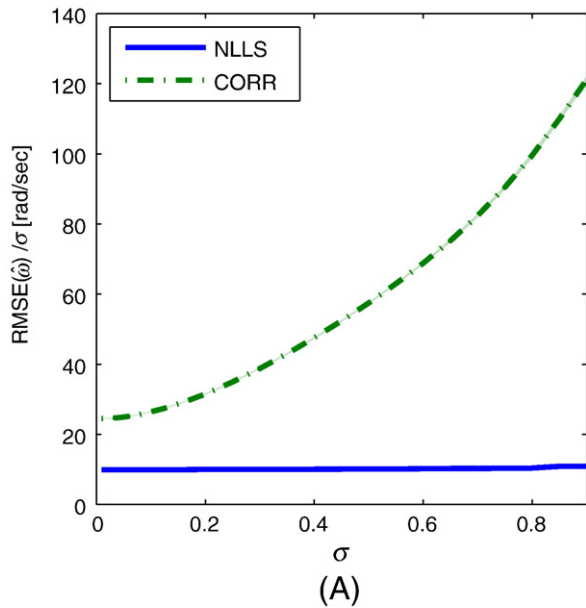


Fig. 4. This figure shows the RMSE/ σ of the different methods for the simulated signals with $\omega=30$ rad/s (A) or $\omega=180$ rad/s (B). Also, for these results $N=64$, $M=100\,000$ and the shaded areas represents the 95% confidence regions of the scaled RMSE. These figures show the RMSE divided by σ to demonstrate the difference between the methods more clearly.

encoding scheme is replaced by the phase encoding of a conventional GRE sequence [8], so a k-space line is sampled N times after an excitation pulse.

When all k-space lines for each echo number are combined, N images can be reconstructed by Fourier transforming each read-phase plane of the data cube. Each image j (with $j=0, \dots, N-1$) has a different echo time $t_j=t_0+jT_r$, where t_0 is the time between the radio pulse and the center of the first echo and T_r is the time between two subsequent gradient echoes, see (Fig. 1B). The differences between these images recorded with different echo times are caused by relaxation, odd/even

phase shift, and the off-resonance frequency $\omega(\mathbf{r})$. When T_r is small enough to ignore relaxation and field inhomogeneity effects during the readout of a single line, the model of the FFT reconstructed GRE images I is given by

$$I(\mathbf{r}, j) = \rho(\mathbf{r}) e^{\left[i\omega(\mathbf{r}) - \frac{1}{T_2^*(\mathbf{r})} \right] t_j + i\phi(\mathbf{r}) \bmod(j,2)}, \quad (4)$$

where \mathbf{r} is the position in the plane, $\phi(\mathbf{r})$ is the phase difference between the even and the odd images, caused by

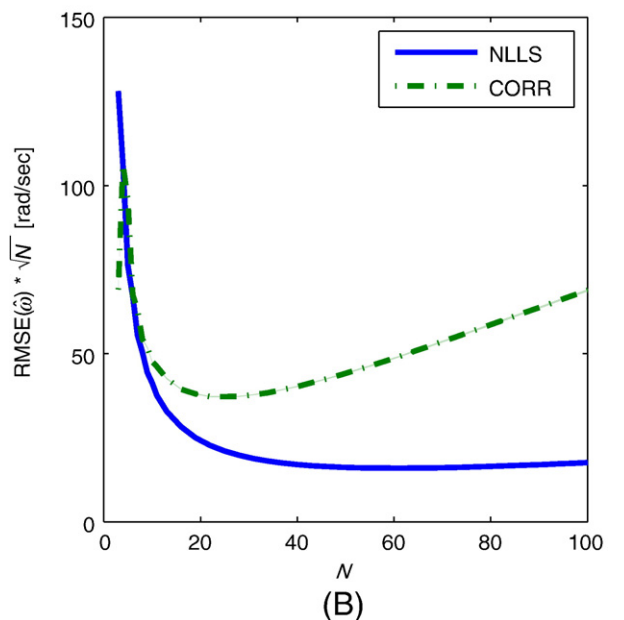
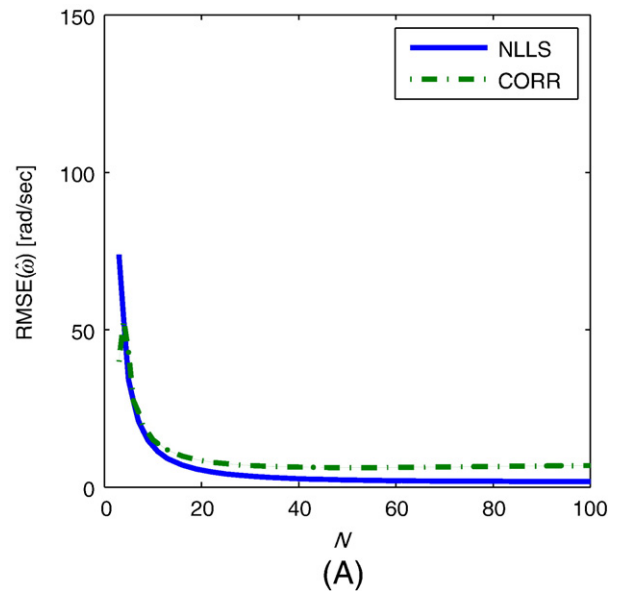


Fig. 5. (A) RMSE and (B) RMSE \sqrt{N} of the different methods for the simulated signals with $\omega=180$ rad/sec. For these results $\sigma=0.2$, $M=100\,000$ and the shaded areas represents the 95% confidence regions of the scaled RMSE.

t_{off} and $\text{mod}(j,2)$ computes j modulo 2, which is zero for even j and 1 for odd j . Although in practice decay of transverse magnetization may be more complex than reflected in the monoexponential form of Eq. 4, this model is expected to be sufficiently accurate, since our aim is to estimate the phase trend $\omega(\mathbf{r})$ from the reference data. The magnitude and phase are orthogonal directions, coupled mainly by the magnitude dependence of the phase variance. Therefore, small errors in the magnitude model will not strongly influence the phase (trend) estimates.

In the next section, an existing method to estimate $\omega(\mathbf{r})$ as well as a new method to estimate $\rho(\mathbf{r})$, $T_2^*(\mathbf{r})$, $\omega(\mathbf{r})$, and $\varphi(\mathbf{r})$ from the reference data will be described.

2.3. Autocorrelation method

The *phase correction method* (CORR) in Ref. [8], a modified version of the method in Ref. [13], uses the autocorrelation function R to estimate the field map. The autocorrelation of a series of N_1 complex values z_j ($j=0, \dots, N_1-1$), without subtracting the mean, is given by

$$R(m) = \begin{cases} \sum_{j=0}^{N_1-1-m} (z_{j+m})(z_j)^* & m \geq 0 \\ R^*(-m) & m < 0 \end{cases}. \quad (5)$$

Due to the even-odd echo asymmetry, the even and odd echo images are processed separately:

$$z_{\text{even},j}(\mathbf{r}) = I(\mathbf{r}, 2j) \quad (6a)$$

$$z_{\text{odd},j}(\mathbf{r}) = I(\mathbf{r}, 2j + 1), \quad (6b)$$

where $j=0, \dots, N_1$, with $N_1=[N/2]$ for z_{even} and $N_1=[N/2]$ for z_{odd} . From these two time series, for each voxel, R_{even} and R_{odd} are computed, where the position argument \mathbf{r} is not shown to simplify notation. The phase trend is present in $\Phi[R(1)]$, where Φ returns the phase of a complex value. The estimator of the off-resonance frequency $\omega(\mathbf{r})$ is then given by

$$\omega_{\text{CORR}}(\mathbf{r}) = \frac{\Phi[R_{\text{even}}(1)] + \Phi[R_{\text{odd}}(1)]}{4T_r}. \quad (7)$$

Note that this procedure does not account for relaxation.

2.4. Nonlinear least squares estimator

Our proposed *nonlinear least squares* (NLLS) method to estimate $\omega(\mathbf{r})$ is based on the complex valued data model from Eq. (1). In order to use real-valued optimization routines, which are most common, the function is re-parameterized for each position \mathbf{r} as

$$f[j, \boldsymbol{\lambda}(\mathbf{r})] = e^{i[\lambda_1 j + \lambda_2 + \lambda_3 \text{mod}(j,2)] + \lambda_4 j + \lambda_5}, \quad (8)$$

with

$$\boldsymbol{\lambda} = [\lambda_1, \dots, \lambda_5] \quad (9)$$

$$= \left[\omega(\mathbf{r})T_r, \Im\{\ln \rho(\mathbf{r})\}, \varphi, -\frac{T_r}{T_2^*}, \Re\{\ln \rho(\mathbf{r})\} \right], \quad (10)$$

where $\Re\{\}$ and $\Im\{\}$ return the real and imaginary part of a complex value, respectively. For each position \mathbf{r} , the

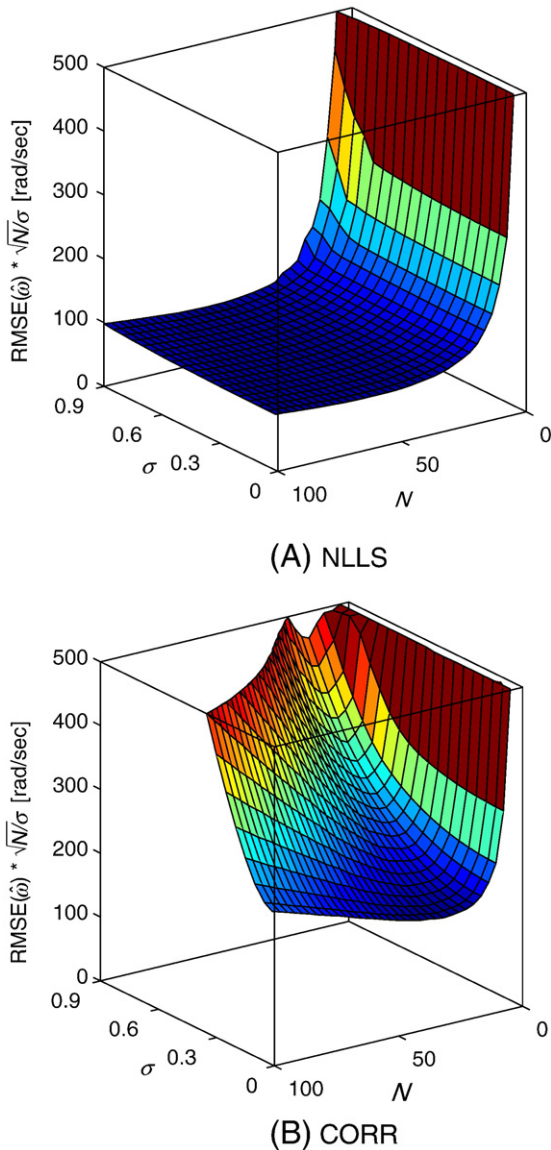


Fig. 6. scaled RMSE of the NLLS (A) and (B) estimators as function of σ and N . To more easily compare the results the scaled RMSE is limited to 500. The actual scaled RMSE of (B) is actually (much) higher than 500 for large N and σ . for each point the number of repetitions is $M=10000$.

function $f(j, \boldsymbol{\lambda})$ is fitted to the N data points $I(\mathbf{r}, j)$ in a least squares sense, with respect to $\boldsymbol{\lambda}$:

$$\hat{\boldsymbol{\lambda}}(\mathbf{r}) = \arg \min_{\boldsymbol{\lambda} \in \mathbb{R}^5} \sum_{j=0}^{N-1} |f(j, \boldsymbol{\lambda}) - I(\mathbf{r}, j)|^2, \quad (11)$$

where the $\hat{\cdot}$ indicates an estimated value. The NLLS estimate of the off-resonance frequency $\omega(\mathbf{r})$ is then given by

$$\omega_{\text{NLLS}}(\mathbf{r}) = \frac{\hat{\lambda}_1}{T_r}. \quad (12)$$

During the optimization, no constraints are applied. However, due to the periodicity of the exponential function in Eq. (8), the resulting parameter vector estimate $\hat{\boldsymbol{\lambda}}(\mathbf{r})$ given in Eq. (11), can always be mapped to satisfy

$|\lambda_1| \leq \frac{\pi}{2}$, $|\lambda_2| \leq \pi$, and $|\lambda_3| \leq \pi$. Note that the correlation estimator in Eq. (7) produces phase trend estimates $\hat{\omega}T_r$, in the interval $[-\frac{\pi}{2}, +\frac{\pi}{2}]$ as well.

3. Experiments

Simulation as well as imaging experiments were run to compare the *phase correction method* CORR with the proposed NLLS method in terms of the precision and accuracy of the field map estimation. Reference data was simulated and the field map $\omega(\mathbf{r})$ was estimated with both methods. In addition, to test the performance of the estimators with real data, the different field map estimators were compared on experimental EPI images along with reference data.

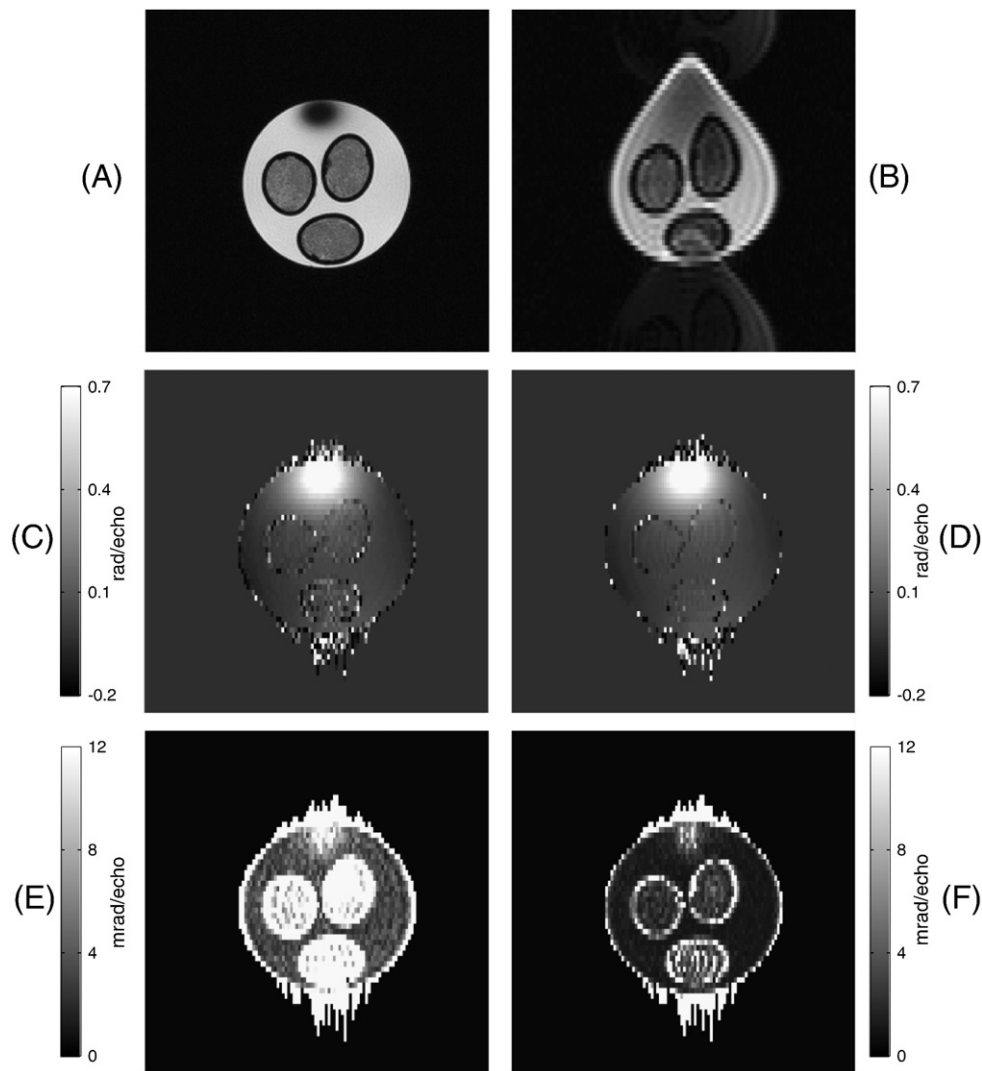


Fig. 7. Field map corrections. The images of the DTI phantom object are acquired at the Bio Imaging Lab with a 7 T Bruker Pharmascan small animal MRI system. Panel (A) shows a Spin Echo image of the phantom. Panel (B) shows an EPI image of the same slice. This image shows a large distortion caused by a nearby air bubble. The panels (C) and (D) show a phase map estimated from reference data of this slice for the CORR and the NLLS method, respectively. The background is masked in the field maps, since the field map cannot be estimated when no signal is present. The panels (E) and (F) show the standard deviation of the field map, computed from 10 acquisitions of the field map reference data, for the CORR and NLLS method, respectively.

3.1. Simulation experiments

In order to test the precision and accuracy of the phase trend estimators as a function of the number of echoes N , the noise standard deviation σ , and the phase trend magnitude ω , several simulation experiments were performed. To this end, two reference data sets were simulated with $T_2^*=30$ ms, $T_r=1$ ms, $\rho=2$, and $\varphi=0.2$ rad, which were held constant throughout all the simulation experiments. The first reference data set was simulated with $\omega=30$ rad/s, which did not cause a phase jump and the second reference data set was simulated with $\omega=180$ rad/s, which caused two phase jumps. Fig. 2A shows the phase of both signals without noise added and with $N=64$, and Fig. 2B shows one simulation of both signals after Gaussian noise with $\sigma=0.2$ was added. The value for ρ and σ should be interpreted in terms of the signal-to-noise ratio (SNR), which is given by

$$\text{SNR} = \frac{P_{\text{signal}}}{P_{\text{noise}}} = \frac{|\rho|^2 \left(1 - e^{-2NT_r/T_2^*}\right)}{2\sigma^2 N \left(1 - e^{-2NT_r/T_2^*}\right)}, \quad (14)$$

where P_{signal} and P_{noise} denote the power of the signal and noise, respectively.

During all simulation experiments, the root-mean-squared-error (RMSE) and the bias of the CORR and NLLS field map estimators were analyzed.

Three Monte Carlo simulations were produced according to the following protocols:

- The first simulation experiment tested the precision and accuracy of the phase trend estimators as a function of σ . For this, independent Gaussian noise with standard deviation $0 \leq \sigma \leq 0.9$ was added to the real and imaginary parts. In this experiment, the number of echoes was held constant at $N=64$ and the number of Monte Carlo realizations was $M=100\,000$.
- The second simulation experiment investigated the effect of changing the number of echoes $3 \leq N \leq 100$. In this simulation experiment, the noise level was fixed to $\sigma=0.2$ and the number of Monte Carlo realizations was $M=100\,000$. Since the signal decays, the SNR will depend on the number of echoes N . The CORR and NLLS methods were again used to estimate ω .
- In the third simulation experiment, both the number of echoes N and the standard deviation σ were varied, where $3 \leq N \leq 100$ and $0 \leq \sigma \leq 0.9$ and the number of Monte Carlo realizations was $M=10\,000$.

3.2. Imaging experiments

In order to investigate the performance of the methods on real data, three different datasets of a DTI hardware phantom were acquired with a 7T Pharmascan small animal system, manufactured by Bruker (Ettlingen, Germany). The DTI

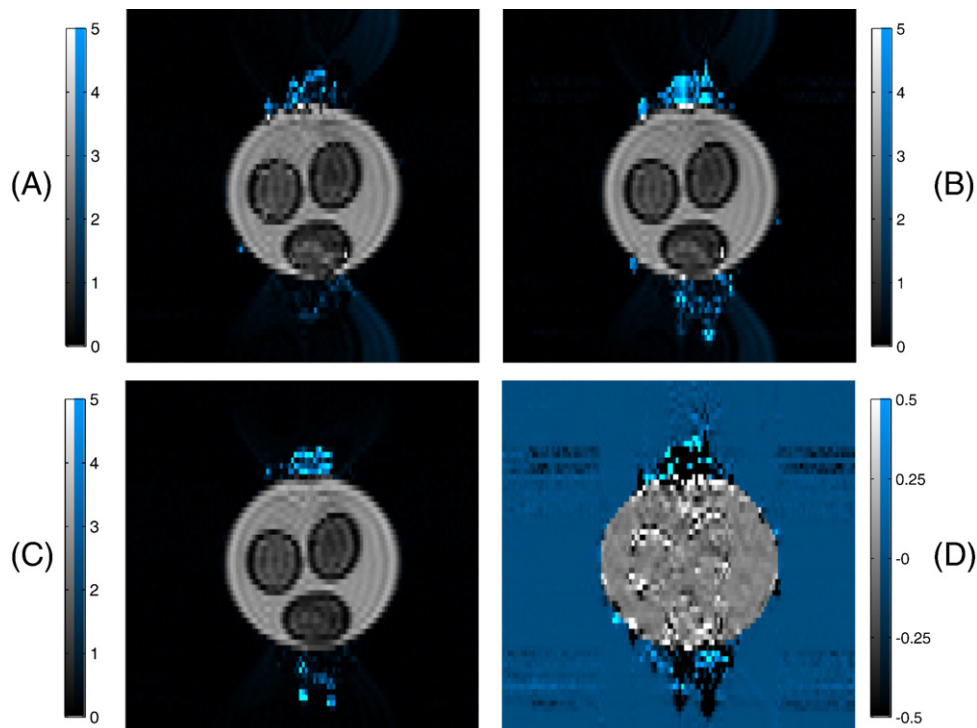


Fig. 8. This figure shows the field map correction results. Panels (A) and (B) show the EPI image corrected with the field maps computed with the CORR method and NLLS method, respectively. Outside the object, the field map cannot be estimated, and thus the image cannot be corrected outside the object. Therefore, a blue color mask is applied outside the object to indicate that any signal in these regions is not relevant. In panel (C), the ghost that is present in panel (B) is suppressed with the odd-even phase difference estimated by the NLLS method. Panel (D) shows the difference between (A) and (B).

hardware phantom consists of parallel bundles of woven strands of Micro Dyneema fibers [14]. The first set was a DTI dataset, which was recorded with an EPI sequence ($TE=35$ ms, $TR=3000$ ms, imaging matrix= 128×64). This data set contained substantial geometric distortions due to susceptibility artifacts (see Fig. 7B).

To enable the correction of these geometric distortions, reference data, as described in subsection 2.2, were recorded with the same parameters. To be able to compare the quality of the estimated field maps, the acquisition of the reference data was repeated 10 times, with an artificially increased noise level to more clearly identify the effects of the noise on the estimated field maps. For these reference datasets, the number of echoes N in the multi echo gradient echo (GRE) sequence equals the number of phase encoding steps of the EPI sequence. Hence, for each reference dataset, $N=64$ GRE images with different echo times were acquired.

To validate the correction results, a 256×128 SE image was recorded with $TE=43$ ms, $TR=1500$ ms. Since an SE sequence is less sensitive to susceptibility artifacts than EPI, the image recorded with this SE sequence can serve as a suitable basis for comparison of the corrected EPI image. For all data sets, 20 slices of 1 mm thickness were acquired and the field of view was 45 mm.

3.3. Implementation details

For all simulations and experiments presented in this paper, MATLAB (The MathWorks, Natick, MA, USA) was used with custom routines. The optimization of the NLLS method used the standard nonlinear least squares routine (lsqnonlin).

This routine is a local optimization routine, and thus there is no guarantee that the global minimum will be found. However, when the initial values are sufficiently close to the position of the global minimum, the routine will converge to that. In the remainder of this paper, a Fourier based initialization of λ was employed. It was observed that with this initialization the global minimum was almost always found, especially for low σ . Furthermore, note that a good initialization will decrease the number of iterations needed to reach the optimum. At our machine (2.4-GHz Intel Core 2 Quad CPU), the initialization and estimation procedure took approximately 9.6 ms per voxel.

4. Results and discussion

4.1. Simulation experiments

This section discusses the results of the simulation experiments described in subsection 3.1.

4.1.1. Performance as a function of the noise level

Fig. 3 shows the RMSE as well as the bias of the field map estimators as a function of σ for the first data set ($\omega=30$ rad/s) with $N=64$. The lines in the figures indicate the observed values and the shaded areas represent the 95%

confidence intervals. Fig. 3A shows that the bias of the CORR and the NLLS estimator cannot be proven to be nonzero in this simulation.

Fig. 3B shows that the RMSE of the NLLS estimator is substantially smaller than the RMSE of the correlation estimator for all noise levels. Note that the RMSE of both estimators is mainly caused by the variance of the estimators, not by the bias. Hence, the increase of the RMSE visible in Fig. 3B is mainly due to the increasing noise level.

The scaling of the RMSE as a function of σ obscures the relative performance of the different estimators. Therefore, to compensate for the expected relation between RMSE and noise level, Fig. 4A shows the RMSE scaled by $1/\sigma$. Note that, for the NLLS estimator, the scaled RMSE is constant, which indicates constant efficiency of the estimation of the field map by this estimator. On the other hand, the scaled RMSE of the CORR estimator increases with increasing σ , which indicates that the estimator becomes less efficient with increasing noise level.

Fig. 4B shows the results when phase jumps are present in the data. Comparison of Fig. 4A and B shows that the RMSE of CORR and NLLS estimators are not significantly influenced by the phase jump.

4.1.2. Performance as a function of the number of gradient echoes

Fig. 5 shows the performance of the field map estimators as a function of N . Fig. 5A shows the RMSE while Fig. 5B shows this RMSE scaled by \sqrt{N} to remove the main trend of the RMSE. As can be seen in Fig. 5B, the RMSE of the estimators sharply decreases with N , when N is small. Then, it levels off and for large N the scaled RMSE starts to increase again. Note that the RMSE itself, however, does not increase, even for large N . This decrease and increase of scaled RMSE is expected. First, the scaled RMSE decreases with increasing number of echoes, since the linear trend of the phase of the simulated series of echoes is estimated. To accurately estimate a linear trend, the samples should be separated by as large a distance as possible. Therefore, increasing the maximum distance between the samples by adding an extra sample (i.e. record an extra echo) decreases the (scaled) RMSE. Secondly, when the number of echoes is increased beyond a certain limit, the scaled RMSE increases. This is also expected, since the magnitude of ρ is fixed and each subsequent echo has a lower magnitude due to the T_2^* relaxation. Beyond a certain number of echoes, the magnitude will be so low that the amount of information added by each subsequent echo is less than expected by the scaling, which assumes a constant amount of information per echo.

4.1.3. Performance as a function of noise level and number of echoes

Fig. 6 shows RMSE \sqrt{N}/σ , where both N and σ are varied and where the scalings of the previous figures are combined. Fig. 6A shows that the scaled RMSE of the NLLS

estimator is (approximately) constant for a large part of the parameter space ($N > 20$). This is not the case for the CORR estimator, as can be seen in Fig. 6B. By comparing Fig. 6A and B, one can clearly see that the RMSE of the NLLS estimator is much smaller than that of the CORR estimator for any N and σ .

4.2. Experimental data

Fig. 7 shows the results of the recorded experimental MRI data. Fig. 7A shows an SE image of the DTI phantom. This image serves as a suitable basis for comparison of the corrected EPI images. Fig. 7B shows the corresponding, original reconstructed EPI image. In this EPI image, a large distortion is visible due to an air bubble located a few slices away, as well as a significant ghosting artifact. Fig. 7C shows the field map obtained with the CORR method and Fig. 7(D) shows the field map obtained with the NLLS method. Comparing these images demonstrates that the NLLS method is less sensitive to magnitude differences, as the noise inside the (darker) fiber bundles is clearly lower for the NLLS method. This is more clearly visible in Fig. 7 (E) and (F), which show the standard deviation of the field map of the CORR and NLLS method, respectively. This standard deviation map is computed from 10 complete acquisitions of the reference data. From each of the 10 reference data sets a field map is computed and after subtraction of the median of each field map, the standard deviation of the field map is computed for each pixel. Fig. 8 demonstrates the corrected version of the EPI image Fig. 7B. Since the field map can only be estimated inside the object, a blue color filter is applied to the signal of the corrected images outside the object, as any signal in this region is due to off resonance effects of parts of the object and an object mask can be used to remove these spurious signals. Fig. 8A and B show the results of the application of the correction scheme to the EPI image with the field map $\hat{\omega}_{\text{COR}}(\mathbf{r})$ and $\hat{\omega}_{\text{NLLS}}(\mathbf{r})$, respectively. Since no ghost correction is applied in these images, the ghost is clearly visible. In Fig. 8C, the even-odd phase difference, which is also estimated by the NLLS estimator, is used to suppress the ghost artifacts still present in Fig. 8B. Fig. 8D shows the difference between Fig. 8A and B. As is clearly visible, the largest differences are at the low signal regions around the fiber bundles. In these regions, the correction with $\hat{\omega}_{\text{COR}}(\mathbf{r})$ is significantly worse.

In summary, Fig. 7 and Fig. 8 clearly show the superior performance of the NLLS estimator.

4.2.1. The reference data needed

The off-resonance map is generally a smooth function of the spatial coordinates. Hence, the spatial resolution with which the field map, and thus, the reference data, has to be acquired, may be lower than the resolution of the images that need to be corrected. Moreover, scan time can be reduced by reducing the number of gradient echoes recorded for the reference data. As is shown in

Fig. 5, the performance of the NLLS estimator improves substantially up to approximately 20 echoes, and for higher N scales with approximately $1/\sqrt{N}$. A further aspect that might be exploited to minimize the reference data scan time is that the reference data does not need to have the same image contrasts as the images to be corrected. As long as the field inhomogeneities are equal, the field map obtained from the reference data can be used for images with different contrasts. Finally, we remark that the substantially improved precision of the proposed NLLS field map estimator compared to the CORR estimators can as well be traded for a faster acquisition of the reference data with reduced SNR (e.g., by reducing TR).

5. Conclusions

High-speed acquisitions such as EPI, are desirable for techniques like DTI and fMRI. Unfortunately, such acquisitions suffer from serious geometrical distortions, especially at high main magnetic fields. Therefore, correction methods which reduce these distortions are necessary. Such methods estimate the field map, which captures the local magnetic field inhomogeneities. The quality of corrected EPI images depends on the precision and accuracy with which the field map is estimated.

In this work, NLLS was described to estimate the field map. Compared to a previously proposed estimation method by Smithorst et al. [8], the proposed NLLS was shown to perform substantially better in terms of the root mean squared error of the estimated field map and, thus, lead to higher quality of the corrected EPI images.

A further benefit of the NLLS estimator is that other parameters of the MR image are simultaneously estimated. These parameters, which include the relaxation and the ghost causing odd/even k-line differences, can be used to correct the ghosting and T_2^* blurring.

Acknowledgments

This work has been financially supported by the I.W.T. (Institute for Science and Technology-Belgium; SBO Quantiviam).

References

- [1] Mansfield P. Multi-planar image formation using NMR spin echoes. *J Phys C* 1977;10:L55–8.
- [2] Mori S, van Zijl P. Fiber tracking: principles and strategies — a technical review. *NMR Biomed* 2002;15:468–80.
- [3] Basser P, Jones D. Diffusion-tensor MRI: theory, experimental design and data analysis — a technical review. *NMR Biomed* 2002;15: 456–67.
- [4] Gruetter R. Localized in vivo adjustment of all first-and second-order shim coils. *Magn Reson Imaging* 1993;20:801–11.

- [5] Zhao Y, Anderson A, Gore J. Computer simulation studies of the effects of dynamic shimming on susceptibility artifacts in EPI at high field. *J Magn Reson Imaging* 2005;173:10–33.
- [6] Tao G, He R, Poonawalla AH, Narayana P. Nonlinear image registration with voxel adaptive regularization to correct for EPI-induced geometric distortions. *Proc. ISMRM*; 2007. p. 986.
- [7] Jezzard P, Balaban R. Correction for geometric distortion in echo planar images from B_0 field variations. *Magn Reson Med* 1995;35:65–73.
- [8] Schmithorst V, Dardzinski B, Holland S. Simultaneous correction of ghost and geometric distortion artifacts in EPI using a multiecho reference scan. *IEEE Trans Med Imaging* 2001;20(6):535–9.
- [9] Chen N, Wyrwicz A. Correction for EPI distortions using multi-echo gradient-echo imaging. *Magn Reson Med* 1999;41:1206–13.
- [10] Zaitsev M, Hennig J, Speck O. Point spread function mapping with parallel imaging techniques and high acceleration factors: Fast, robust, and flexible method for echo-planar imaging distortion correction. *Magn Reson Med* 2004;52:1156–66.
- [11] Robson M, Gore J, Constable R. Measurement of the point spread function in MRI using constant time imaging. *Magn Reson Med* 1997;38:733–40.
- [12] Haacke E, Brown R, Thompson M, Venkatesan R. *Magnetic Resonance Imaging – Physical Principles and Sequence Design*. New York: John Wiley & Sons; 1999.
- [13] Ahn CB, Cho ZH. A new phase correction method in NMR imaging based on autocorrelation and histogram analysis. *IEEE Trans Med Imaging* 1987;MI-6:32–6.
- [14] Fieremans E, Delpitte S, Deblaere K, De Deene Y, Truyens B, D'Asseler Y, et al. A flexible hardware phantom for validation of diffusion imaging sequences. *Proceedings ISMRM, Miami*; 2005. p. 1301.
- [15] Grieve S, Blamire A, Styles P. Elimination of nyquist ghosting caused by read-out to phase encode gradient cross-terms in EPI. *Magn Reson Med* 2002;47:337–43.